Ocean current observations from Nares Strait to the west of Greenland: Interannual to tidal variability and forcing

by Andreas Münchow[1] and Humfrey Melling[2]

ABSTRACT

During 2003–06, as part of the Arctic Sub-Arctic Ocean Flux (ASOF) experiment, an array of ocean-sensing instruments was deployed at 80.5N latitude to investigate the flux of seawater from the Arctic Ocean via Nares Strait, the pathway to the west of Greenland. Three-year measurements of current from this experiment provide, for the first time at periods longer than a single season, the seawater flux and its variability via this important pathway. Below 30-m depth the average flux of volume 2003–06 was 0.57 ± 0.09 Sv (1 Sv $= 10^6$ m^3 s^{-1}) southward over a 38-km wide section reaching 360 m in depth. A linear trend, statistically significant at the 95% confidence level, indicates an increase in the sectionally averaged flow below 30-m depth of $20 \pm 10\%$ between 2003 and 2006. The flow is dominated by mixed diurnal and semi-diurnal tidal currents with kinetic energy an order of magnitude larger than that of the subtidal flow. The range of seasonal variation is 30–50% of the long-term mean flow. Variations in flow of daily to monthly period are comparable in magnitude to the average flow. The flow through the cross-section is the net result of a larger southward flux in the deep western two thirds of the strait and a small northward flux within about 5 km of Greenland. The latter is about 5% of the former. Spectral analyses indicates that the cross-channel pressure gradient is highly correlated with the sectionally averaged flow consistent with geostrophy. Along-channel pressure gradient explains 70% of the variance at a 33-day period with a phase lag consistent with a frictional response; at 3–7 day period the response is weaker ($<30\%$) with a phase relation suggestive of contributions by both friction and local acceleration.

1. Introduction

The Canadian Archipelago and Fram Strait (Fig. 1) constitute the two pathways for the exchange of water and ice between the Arctic and Atlantic oceans (Melling *et al.*, 2008; White *et al.*, 2007; Serreze *et al.*, 2006). Arctic outflows via these pathways return freshwater to the North Atlantic that was evaporated from tropical oceans, transported by the atmosphere, and delivered to the Arctic Ocean via inflow from the North Pacific, via

1. College of Marine and Earth Studies, University of Delaware, Newark, Delaware, 19716, U.S.A. *email: muenchow@udel.edu*
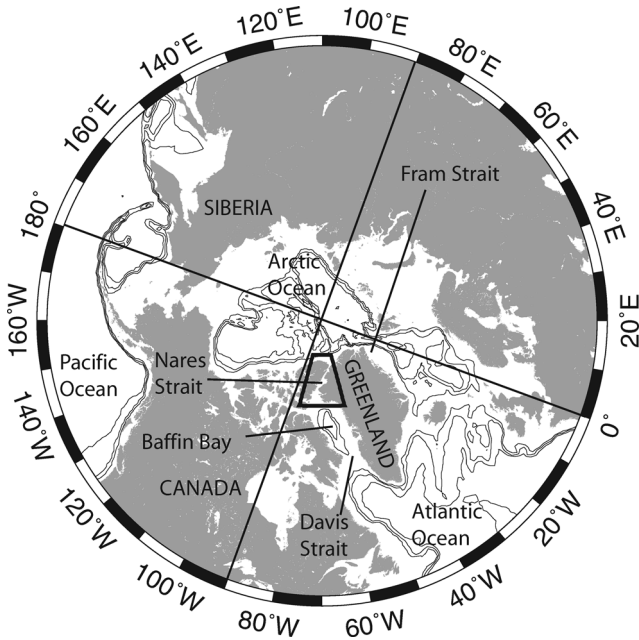2. Institute of Ocean Sciences, Sidney, British Columbia, Canada.

Figure 1. Map of the northern hemisphere with the study area.

precipitation, and via terrestrial run-off (Warren, 1983; Emile-Geay *et al.*, 2003). Here we focus on through-flows west of Greenland via Nares Strait which is a major conduit southward into Baffin Bay and the Atlantic Ocean. Fluxes through Nares Strait may reflect the impacts of diminishing sea ice in the Arctic (Parkinson and Cavalieri, 2008), disintegrating ice shelves of northern Canada (Copland *et al.*, 2007; Nutt, 1966), and potentially surging glaciers of northern Greenland (Rignot and Steffen, 2008). Numerical global climate scenarios appear sensitive to the parameterization of both the physical processes and pathways of Arctic to sub-Arctic exchange of water (Curry and Mauritzen, 2005) and vorticity (Yang, 2005). More specifically, the presence of Arctic outflows both west and east of Greenland appears to improve model performance relative to those climate models without a Canadian Archipelago (Holland *et al.*, 2007).

The interaction between Arctic and Atlantic oceans via Nares Strait resembles the discharge of buoyancy (freshwater) from a reservoir (the Arctic) into a receiving basin (the Atlantic) via a channel of finite length (Nares Strait). In studying buoyant discharge into the ocean, Garvine (1987, 1995) used a Kelvin number $K = W/L_D$ to represent the importance of Earth's rotation in the dynamics. Here W is a cross-stream length scale (e.g. channel width) and L_D is the internal Rossby radius of deformation. For large Kelvin numbers, such outflows are often coastally trapped both within the channel and the adjacent receiving basin. Reviewing the regional circulation, LeBlond (1980) also emphasized the importance

of K and commented that the main channels of the Canadian Arctic Archipelago such as Nares Strait are wide enough to accommodate counter-flowing geostrophic flows in the upper layer along both coasts. Two decades later, Münchow *et al.* (2006, 2007) presented detailed snapshots of flow structure on four cross-sections of Nares Strait based on velocity surveys of high spatial resolution. Numerical models of circulation in Baffin Bay, linking Nares Strait to the Labrador Sea, have also revealed strong and narrow boundary currents flowing in the direction of Kelvin wave propagation (Dunlap and Tang, 2006; Kliem and Greenberg, 2003), although the inflows to the model domain, such as via Nares Strait, were poorly known.

Observational work in Nares Strait has been impeded by the remote location, harsh climate, and unpredictable summer ice conditions. Sadler (1976) and Bourke *et al.* (1989) observed temperature and salinity in Nares Strait in the summers of 1971 and 1986, respectively. However, these early studies primarily illustrate hydrographic variability along, not across the strait. Although it is generally believed that Nares Strait carries between 30 to 50% of the total flux through the Canadian Archipelago (Prinsenberg and Hamilton, 2005; Dickson *et al.*, 2007), observations of flow have been harder to obtain. Sadler (1976) reported vertically resolved currents from a deployment of three moorings for six weeks in the late winter of 1972. His derived estimates of volume, freshwater, and heat fluxes through Nares Strait have been widely quoted, employed as boundary conditions in numerical models, and used to constrain Arctic Ocean budgets (Serreze *et al.*, 2006). However, more than half the volume flux was attributed to a single instrument at 100-m depth within 5 km of the Ellesmere Island coast. Melling *et al.* (2001) presented 10-month long current meter mooring records from a 1997–98 North Water project at the southern entrance to Nares Strait, but concluded that data from two moorings across 40-km wide Smith Sound were inadequate to derive volume flux.

This study presents results based on a three-year record of flow through Nares Strait acquired using instruments on sub-sea moorings. We here follow a conventional approach to the analysis of time series from such instruments, namely to ignore flow in a zone just beneath the surface. Generally in oceanographic observational studies, measurements are not acquired by moored instruments within the near-surface zone because of risk to installations from wind waves, shipping, fishing, or in our case, ice. Nor have we attempted to extrapolate our existing observations up to the surface, in acknowledgement of possible strong shear across this zone. Such shear is likely in the presence of the strong vertical density gradient associated with surface freshwater admixture characteristic of Arctic waters. We provide here estimates of the long-term average volume flux (at depths beneath the surface layer) of Arctic waters toward Baffin Bay and discuss the variability of this flow at periods ranging from tidal to inter-annual. We introduce observations of along- and across-channel pressure gradients and estimates of along-channel wind to explore the forcing and control of flow through the channel. Our analyses form a baseline against which to discuss sparse prior measurements of Canadian Arctic through-flow and to evaluate future change.
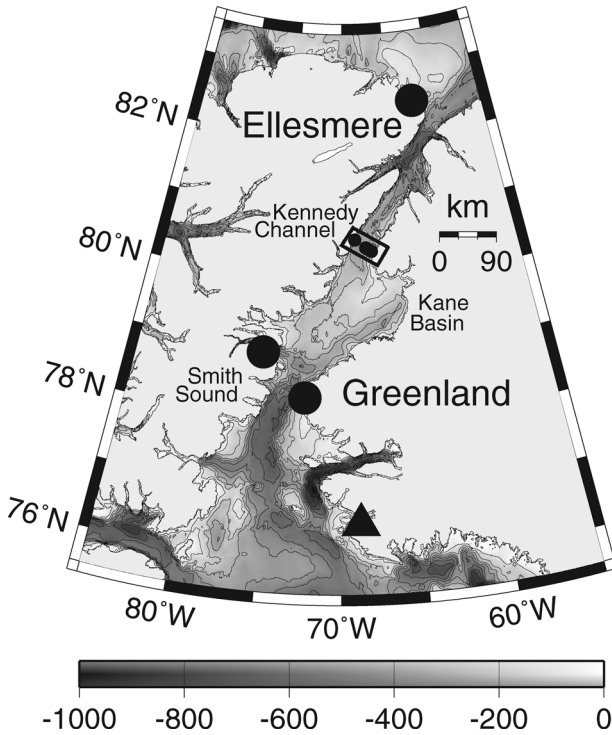
Figure 2. Map of the study area with instrument locations. The triangle indicates the location of Thule at Pituffik, Greenland while the large circles indicate the locations of, from south to north, the bottom pressure at Foulke Fjord, Greenland, bottom pressure at Alexandria Fjord, Ellesmere Island, and tide gauge station at Alert, Ellesmere Island, Canada. The ADCP mooring locations at the southern end of Kennedy Channel are indicated by small circles inside the polygon at 80.5N latitude. Contours are bottom depth in 100-m increments to 1000 m.

2. Study area and data

Nares Strait is the channel that separates Greenland from Canada between 78N and 82N latitude (Fig. 2). It borders the Canadian Archipelago and is more than 500-km long with width varying from about 21 km in the north (Robeson Channel) to 50 km in the south (Smith Sound). The depth of water along the axis of the strait decreases from about 600 m in Smith Sound to 220 m at the sill in western Kane Basin and then increases again to about 800 m in Hall Basin. The area is generally ice covered with rapidly drifting multi-year ice floes in summer (Fig. 3) and with stable land-fast ice, a mixture of multi-year and annual forms, in winter (Fig. 4). The land-fast ice stabilizes behind an ice bridge that usually forms some time between December and March in Smith Sound (Dunbar, 1973; Kwok, 2005). Nares Strait receives icebergs calved from the Greenland ice sheet via the Petermann Glacier which discharges into Hall Basin and via the Humboldt Glacier that discharges into Kane Basin (Fig. 2).
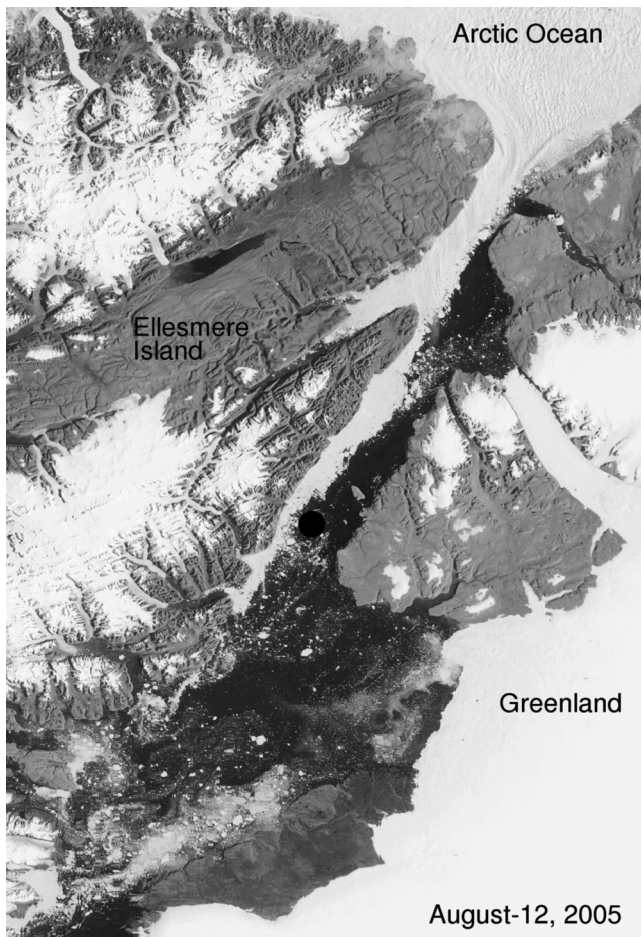
Figure 3. MODIS image of Nares Strait on August 12th, 2005. The dot indicates the location of the mooring section.

An array of autonomous instruments on sub-sea moorings was deployed across a 38-km wide cross-section of Kennedy Channel in August 2003. It was recovered in part in August 2006 (Fig. 5). There were 17 moorings on this section, 8 carrying temperature-salinity recorders at four levels, 2 carrying ice-profiling sonar and 7 carrying Doppler sonar for measurement of ocean current and ice drift. The latter provided the data that are the focus of the present discussion. Each of these moorings carried an acoustic Doppler current profiler (Long Ranger model operating at 75-kHz, from Teledyne RD Instruments Inc.). The data from an eighth instrument deployed close to the Canadian shore about 50 km north of the main study line, are not discussed here.

Figure 4. MODIS image of Kennedy Channel, Kane Basin, and Smith Sound on April 29th, 2005. The dot indicates the location of the mooring section. Note the presence of the ice bridge that separates land-fast ice in Kane Basin and Nares Strait to the north from the open water (black) with thin new ice forming (grey) in the south. The dot indicates the location of the mooring section.

A magnetic compass is an unreliable heading reference in Nares Strait, which is only a few hundred kilometers from the north magnetic pole. We mounted each ADCP on a torsionally rigid mooring that held it on a fixed azimuth during deployment, while permitting pitch and roll in response to the force of current (Fig. 6). In addition to the four-beam ADCP, mounted on top of a 30-inch steel float, the mooring carried two external battery cases (providing capacity for four-years operation), one SBE37 temperature salinity recorder and two Benthos 866A acoustic transponding releases on the torsionally rigid backbone. The buoyant assembly was connected via a universal joint to the deadweight anchor. Because each mooring was dropped from the surface on deployment, the reference heading of the ADCP, although fixed for the deployment on landing on the seabed, was unknown. Appendix A outlines the method used to determine the true heading through analysis of the measured tidal currents which are closely aligned to the geographic orientation of Nares Strait.
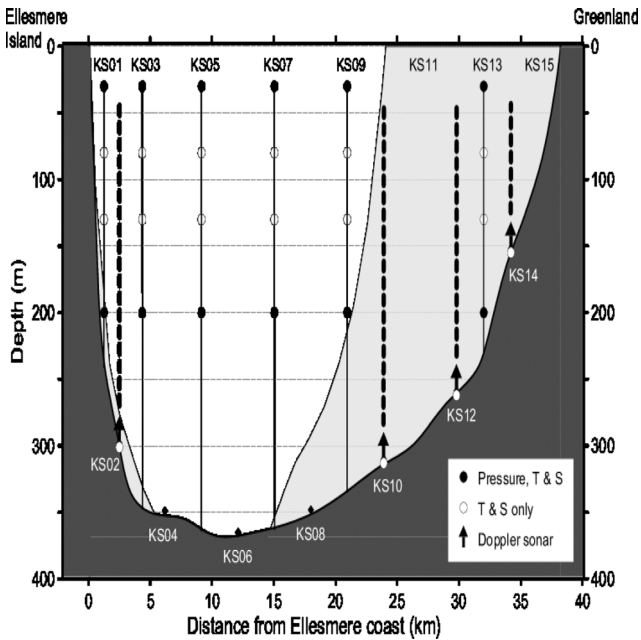
Figure 5. Locations and depths of instruments on the moorings of the Kennedy Channel South (KS) section that were recovered in 2006. The locations of moorings not recovered (KS04, KS06, KS08, KS11, KS15) are also indicated. Light background shading indicates the part of the section blocked by the constriction of Kennedy Channel at Franklin Island, 30 km to the northeast. See Figure 2 for geographic locations.

Ocean current was not determined at times when the amplitude of the received echo was low: each echo originates via backscatter from zooplankton, whose abundance declines dramatically during the polar night and whose diel migration leads to short intervals of data loss every day year round. Data were also lost at times of rapid drift when high ambient noise generated by ice-floe collisions obscured faint echoes; such events were most common in the summer and autumn. Appendix B outlines the procedures for data processing and the method used to interpolate across data gaps resulting from low signal to noise ratio in order to obtain a nearly continuous record for time series analysis.

The ADCPs recorded data twice hourly, providing ocean current averaged over 8-m increments of depth from about 30 m below the surface to 15 m above the seafloor. Table 1 summarizes the data obtained. Unfortunately the second, third and fourth instruments (numbered from the Canadian shore: sites KS04, KS06, and KS08) were not recovered, thereby leaving a 21-km wide gap without data between the site KS02, 2 km from Ellesmere Island and site KS10 more than halfway to Greenland. All four recovered ADCPs on this section delivered a full three-year data record. Data acquired by ADCPs within a certain distance of the sea surface are contaminated by interfering surface echoes and typically cannot be used.
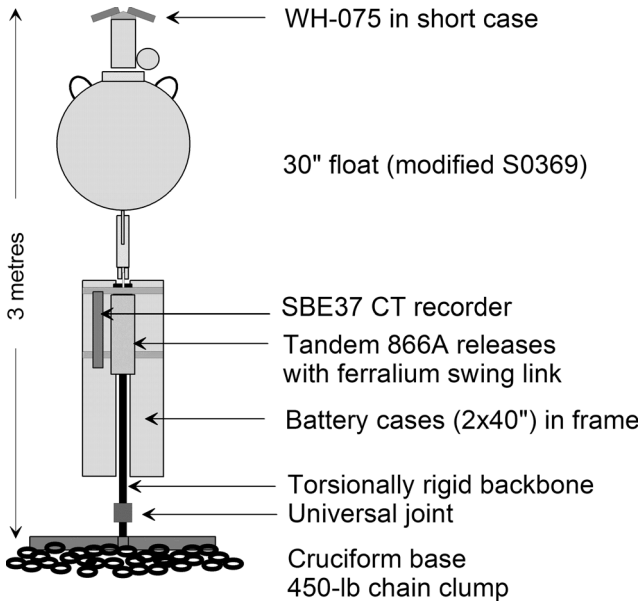
Figure 6. Sketch of the torsionally rigid ADCP mooring design.

Hence we distinguish between vertically averaged currents over the range of depths wherein velocity was measured from a depth-average that incorporates estimates from unobservable zones close to the surface and the seabed. Appendix C describes the uncertainties and biases associated with missing data and the methods used to interpolate across the data voids in the cross-section.

Five pressure recorders were placed at the seabed in shallow bays upstream and downstream of the main array. These recorders contained Digiquartz pressure sensors (Parascientific Inc) accurate to about 0.1 mb. We recorded 30 one second samples every three hours with

Table 1. Mooring location and records.

Name	Longitude, W	Latitude, N	Depth, m	Distance, km	Bins	Angle	Correlation	Record, days
KS02	68.8744	80.5538	302	2.2	32	99.5	0.943	1103
KS04	68.7140	80.5355	357	5.9	n/a	n/a	n/a	0
KS06	68.4540	80.5027	362	11.8	n/a	n/a	n/a	0
KS08	68.1905	80.4715	350	17.8	n/a	n/a	n/a	0
KS10	67.9296	80.4388	299	23.9	32	−58.0	0.970	1105
KS12	67.6709	80.4092	263	29.6	27	−64.7	0.959	1104
KS14	67.4458	80.3884	157	34.4	15	−80.9	0.947	1103
KS16	67.8136	80.7655	368	3.5	40	117.3	0.904	21

the least significant bit representing 0.76 mbar. The largest error results from quantization and is about 0.22 mbar estimated by using a procedure outlined by Bendat and Piersol (1986). Two pressure recorders were recovered, both at the southern end of the strait, at Foulke Fjord, Greenland (78.30N, 72.57W) and at Alexandra Fjord, Canada (78.91N, 75.80W). We also have sea-level data from a tide gauge operated by the Canadian Hydrographic Service at Alert, Canada just west of the northern end of the Nares Strait (82.49N, 62.32W), wherein sea-level pressure data have been applied as correction for the inverted barometer effect (Neumann and Pierson, 1966). Together the three stations provide estimates of the along-channel and cross-channel pressure differences associated with the through-flow.

In the absence of direct wind observations we have used model predictions from a mesoscale atmospheric circulation model (Samelson and Babour, 2008). Filling a six-week gap in February–March 2006, we have reverted to estimates based on a demonstrated linear relationship (Samelson and Babour, 2008) between wind speed and the along-channel difference in atmospheric pressure from Alert to Thule at Pituffik (See Fig. 2 for locations). Sealevel pressure data were acquired from the US National Climate Data Center.

3. Tidal current variations

The tides in Nares Strait are forced by sea-level differences at tidal frequencies between its northern and southern ends. The differences arise from differences in the phase and amplitude between the tidal wave propagating from the North Atlantic and counter-clockwise around the Arctic Ocean to the northern end of Nares Strait and that from the same source propagating counter-clockwise around Baffin Bay (Padman and Erofeeva, 2004). The M_2 amplitude at Alert is 0.20 m (phase of $-33°$), much smaller than the 1.13 m (phase of $-79°$) at Foulke Fjord. In this section we use an analysis of relatively well understood tidal characteristics to demonstrate the validity of the current direction derived via our novel approach to observational challenges near the geomagnetic pole. We work here with vertical averages of the tidal flow. This simplification serves our present purpose, but overlooks important characteristics of the tides that await a future study.

The major diurnal and semi-diurnal constituents are clear in a spectral decomposition of the three-year time series of vertically averaged, along-channel current at KS10; this site is about 14 km from Greenland and 24 km from Ellesmere Island. Figure 7 shows the power spectrum from 0–6 cycles per day (cpd) as well as details for the semidiurnal and diurnal bands where 66.4% and 26.3% of the total variance resides, respectively. We arrive at these percentages by integrating the power spectrum of Figure 7 over successive frequency bands.

For comparison, we show the spectrum of the time series built from 11 major tidal constituents (S_2, L_2, M_2, N_2, μ_2, OO_1, J_1, K_1, M_1, and O_1, and Q_1) whose periods are listed in Table 2 (Neumann and Pierson, 1966). The spectrum of the synthetic time series reveals that spectral leakage from the main peaks does not obscure the four minor constituents (K_2, γ_2, $2N_2$, as well as P_1) within the principal groups. We have used these 15 constituents as
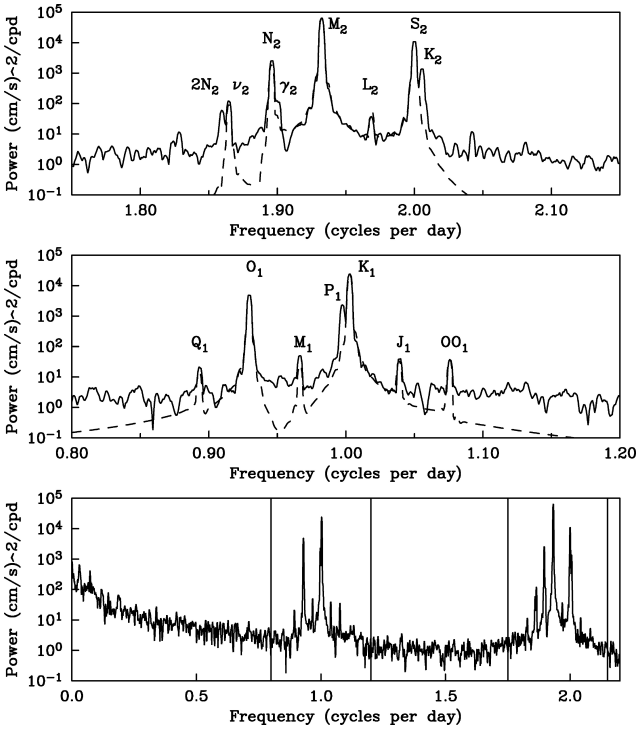
Figure 7. Power spectra of vertically averaged along-channel currents at KS10 for semi-diurnal (top), diurnal (middle), and 0-6 cpd (bottom) frequency bands. Dotted line indicates spectra from artificial time series of 11 major tidal groups with amplitudes close to those determined from harmonic analysis (Table 2).

the basis set for harmonic analysis of tidal current in Nares Strait (Münchow *et al.*, 1992). Estimates of ambient noise (N_a) are required for the estimation of confidence bounds for the constituent data. The spectra in Figure 7 reveal N_a to be about 5 and 10 cm^2 s^{-2} cpd^{-1} for diurnal and semi-diurnal constituents, respectively. The signal-to-noise ratio SNR = $S_0 \sqrt{T/N_a}$ where S_0 is the amplitude of a sinusoidal oscillation and T is the record length. We provide 95% confidence limits as suggested by Filloux and Snyder (1979), because it more accurately provides an upper bound for errors in phase (Münchow *et al.*, 1992).

Table 2 summarizes tidal ellipse parameters and their uncertainties at KS10 for 17 constituents while Tables 3 and 4 show the dominant M_2 and K_1 ellipse parameters for all 5 moorings as determined from a harmonic analysis that includes the largest 7 constituents. At all locations the dominant tidal currents are semi-diurnal, but the diurnal components are substantial. The 7 constituents with amplitudes larger than 3 cm s^{-1} are all oriented $63 \pm 1°$ counter-clockwise from true East along the channel axis. The flow along the major axis reaches 21.4 cm s^{-1} for the dominant M_2 tidal current, and current on the minor axis

Table 2. Tidal ellipse parameters for KS10.

Constituent	Period, hours	Major axis, cm s^{-1}	Minor axis, %	Orientation, °	Phase, °	SNR
M_2	12.42	21.4 ± 0.1	-2	64 ± 0	216	526
K_1	23.93	13.0 ± 0.7	-3	62 ± 6	224	40
S_2	12.00	8.9 ± 0.1	-3	64 ± 1	126	107
O_1	25.82	5.9 ± 0.4	-4	64 ± 8	-58	19
N_2	12.66	4.3 ± 0.1	-5	63 ± 2	138	107
P_1	24.07	3.6 ± 0.8	-8	63 ± 25	34	11
K_2	11.87	3.2 ± 0.1	-5	63 ± 2	13	80
μ_2	12.87	0.8 ± 0.1	-8	62 ± 11	67	3
γ_2	12.62	0.8 ± 0.1	-12	63 ± 9	29	3
$2N_2$	12.91	0.6 ± 0.1	-4	60 ± 8	55	2
M_1	24.86	0.6 ± 0.1	1	52 ± 9	130	2
L_2	12.19	0.5 ± 0.1	3	54 ± 8	116	2
J_1	23.10	0.5 ± 0.1	-15	61 ± 10	-63	2
OO_1	22.31	0.5 ± 0.1	36	74 ± 16	-16	2
Q_1	26.87	0.3 ± 0.0	-27	53 ± 9	-123	1
S_a	8766.16	0.8 ± 0.7	-58	114 ± 45	207	3
S_{sa}	4382.92	0.6 ± 0.2	5	156 ± 72	202	3

Table 3. M_2 Tidal ellipse parameters of vertically averaged currents.

Name	Major axis, cm s^{-1}	Minor axis, %	Orientation, °	Phase, °	SNR
KS02	15.2 ± 0.1	-2	56 ± 0.5	209	392
KS10	21.2 ± 0.1	-2	64 ± 0.3	216	526
KS12	20.9 ± 0.1	-8	67 ± 0.3	218	512
KS14	23.7 ± 0.1	-9	69 ± 0.3	202	577
KS16	21.5 ± 1.0	-2	57 ± 2.8	205	78

Table 4. K_1 tidal ellipse parameters of vertically averaged currents.

Name	Major axis, cm s^{-1}	Minor axis, %	Orientation, °	Phase, °	SNR
KS02	9.1 ± 0.8	-0	57 ± 8.7	218	26
KS10	13.0 ± 0.7	-2	62 ± 5.9	224	40
KS12	12.6 ± 0.7	-4	60 ± 6.5	221	37
KS14	14.1 ± 0.7	-2	60 ± 4.8	227	42
KS16	13.2 ± 7.2	-0	57 ± 59.8	195	5

is always less than 8% of this and negative; the current vector therefore rotates clock-wise around the ellipse, as expected if the Earth's rotation impacts the tidal dynamics via the Coriolis force (Battisti and Clarke, 1982).

Figure 8 depicts the largest semi-diurnal and diurnal tidal ellipses from all 5 mooring locations on a regional map. Tidal currents are uniform both along and across the section at 10 km scales with slightly reduced amplitudes adjacent to the steeply sloping Ellesmere
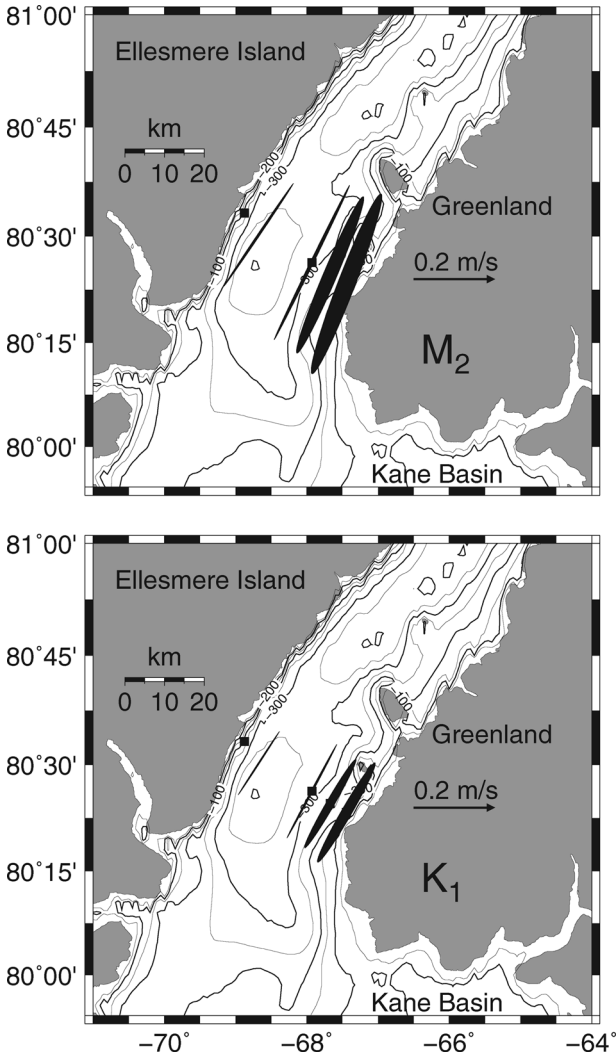
Figure 8. Map of vertically averaged M_2 (top) and K_1 (bottom) tidal current ellipses. The ellipses
for KS02 off Ellesmere Island are offset from their location (dot) towards the channel center for
visibility over the steeply sloping channel. Contours are isobaths in 50-m increments.

Island shore and slightly enhanced across-shore amplitudes inshore of the 300-m isobath
adjacent to the more gently sloping channel off Greenland.

There is substantial vertical variation of the tidal current related to boundary layers near
the bottom and under the ice (not shown). Its description and dynamics is outside the scope
of this study.

Along−Channel, Depth−Averaged Velocity (+ northward)
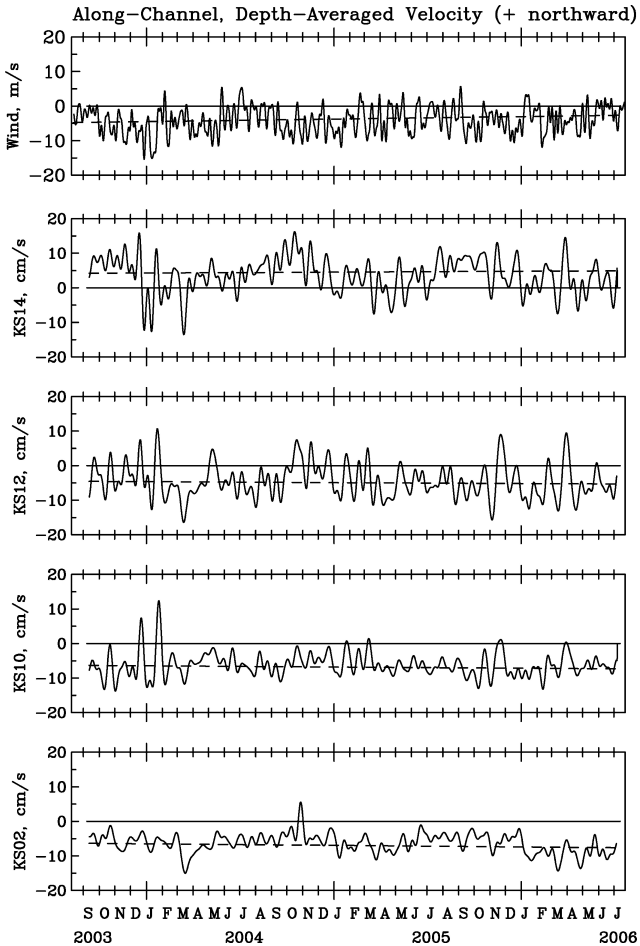
Figure 9. Time series of vertically averaged, low-pass filtered, along-channel velocity from mooring locations off Greenland (KS14, top panel) towards Canada (KS02, bottom panel). A linear regression line is shown by the dashed line. Note the opposing flows off Greenland (northward) with those off Canada (southward).

4. Sub-tidal current variations

a. Overview and time scales

To avoid the complexity of depth variation in the flow, we base the subsequent discussion on vertical averages of the measured flow at each site; depth varies by about a factor of two, between 155 m at KS14 and 302 m at KS02.

Figure 9 displays the measured time series of the vertically averaged along-channel flow near the southern end of Kennedy Channel; along-channel wind is also included. The time

series have been low-pass filtered to retain more than 90% of the variance at periods longer than 20 days and less than 10% at periods longer than 13 days (Lanczos raised cosine filter). This filter transmits about half of the sub-tidal variance and emphasizes monthly variability. Negative (southward) flow prevails at all locations except KS14 near Greenland; here the flow is northward much of the time. Fluctuations and reversals of current are large and frequent near Greenland but diminish towards Canada; they are particular small at KS02. Since the vertically averaged current rarely exceeds 0.1 m s^{-1} in either direction, the larger oscillating tidal currents are generally dominant.

The uncertainty of empirical estimates for statistical properties of the flow (mean, standard deviation, trend, etc.) relates to the decorrelation time, T$_D$ (Kundu and Allen, 1976) which is about a day for the across-channel and 3–4 days for the along-channel component. The time scale is slightly longer at KS02 near Canada than on the Greenland side. Oscillatory behavior in the autocorrelation functions near Greenland (not shown), reaching 0.2 at lags of 10–30 days, indicates coherent variability at weekly to monthly period.

Figure 9 indicates that the flow at KS02 is particular steady, with qualitatively different variability than on the other side of the channel. An empirical orthogonal function (EOF) analysis supports this assessment: the amplitude of the first mode, which explains 69% of the variance, increases from 1.5 cm s^{-1} near Canada to 2.8 cm s^{-1}, 6.0 cm s^{-1}, and 9.6 cm s^{-1} with approach towards Greenland. The second mode is not prominent near Canada (16% of the variance), but the third mode (9% of the variance) is.

Standard EOF analysis only considers in-phase signals. In order to assess the potential of lagged correlated motions, we estimate complex (vector) correlation coefficients of the vertically averaged flow. The lagged correlation of currents at KS02 with the other three stations are always low irrespectively of lag: the maximum values against KS10, KS12, and KS14 are only 0.14, 0.27, and 0.37, respectively.

These results indicate that the vertically averaged, time variable flow near Canada is largely uncorrelated to that observed 20, 25 and 30 km to the east across the strait. With such weak correlation of flow at the measurement sites which bracket the western half of the strait, the uncertainty in volume flux derived by linear interpolation of current between KS02 and KS10 is likely to be large (Appendix C).

b. Interannual time scales

i. Record mean flow and flux. Figure 10 shows the three-year mean of vertically averaged current with 95% confidence limits for both speed and direction. The two variables have been treated as independent, with the assumption that estimates of speed are drawn from a Gaussian normal probability density distribution (Kundu and Allen, 1976) while those of direction are drawn from a von Mises probability density distribution (Mardia, 1972). Table 5 provides numerical and technical details.

Within about 3 km of the Ellesmere Island coast we find a mean vertically averaged flow of 6.7 ± 0.7 cm s^{-1} in a direction $126 \pm 4°$ clockwise from true east (toward the southwest)
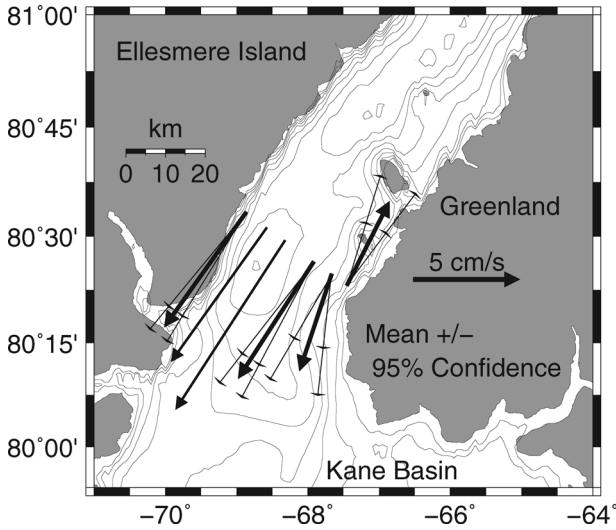
Figure 10. Record-mean vertically averaged flow and its 95% confidence limits for speed and direction (see Table 5 for details). The thinner vectors without confidence limits in the center of the channel represent interpolated currents at KS05 and KS07 (see Appendix C for details). Contours are isobaths at 50-m isobath.

while adjacent to the coast of Greenland at KS14 we find a vertically averaged current of 4.4 ± 1.2 cm s^{-1} in a direction $63 \pm 10°$ counter-clockwise (towards the northeast). The record mean flow at KS02 in the west agrees within 0.1 cm s^{-1} in speed and 3° in direction with the flow at the adjacent mooring location KS10 across a 21 km gap in our array of moorings (Fig. 10). The mean speed, mean direction, and uncertainty at KS12 are similar

Table 5. Statistical parameters related to the record-mean vertically averaged currents. Degrees of freedom (dof) based on the decorrelation time scale T_D, the standard deviation ϵ for speed, and the resultant $R = \sqrt{c^2 + s^2}$ for direction. Here $c = N^{-1} \sum_{i=1}^{N} \cos(\phi_i)$, $s = N^{-1} \sum_{i=1}^{N} \sin(\phi_i)$, and $\phi_i = \phi(t_i)$ is the direction of the flow at time t_i. The mean direction is $\tan^{-1}(s/c)$. R and *dof* determine whether a preferred direction exists via the Raleigh test (Mardia, 1972) and, if it does, the uncertainty of the mean direction. All mean directions exist at the 99.9% confidence level. The 95% confidence limit for speed is $\pm 1.96\epsilon\sqrt{2/dof}$. The 95% confidence limits of the mean direction are from Batschelet's charts as reproduced by Mardia (1972) in his Appendix 2.7a.

Name	Mean speed cm s^{-1}	Mean direction degrees	ϵ cm s^{-1}	R –	dof –	T_D hours
KS02	6.7 ± 0.7	$-126° \pm 4°$	4.3	0.89	277	95
KS10	6.6 ± 0.9	$-123° \pm 5°$	5.2	0.81	259	102
KS12	4.8 ± 1.2	$-108° \pm 12°$	6.7	0.49	258	102
KS14	4.4 ± 1.2	$+63° \pm 10°$	9.6	0.41	491	54

to those at KS02 and at KS10 albeit at speed about 20% less and directed about 5° counter-clockwise towards Kane Basin. The flow at KS12 appears somewhat influenced by Crozier and Franklin islands which are about 15 and 30 km to the north.

The apparent uniformity of mean flow between KS02 and KS10 is fortuitous. Previous study of the spatial cross-section of current through Nares Strait has revealed a baroclinic jet in the western half of the channel (Münchow *et al.*, 2006, 2007). It is very likely that this jet flowed through the 21-km wide gap in the mooring array during 2003–06. In Appendix C we provide quantitative evidence to suggest that flow through the gap was in fact larger than that estimated by linear interpolation between sites of measurement. This justifies our nonlinear interpolation of flow speed across the gap. Figure 10 includes two vectors as estimates of current at KS05 and KS07 which have been derived by scaling adjacent flows upward by factors deduced from the measured pull down by current of tall moorings at these sites; see Appendix C for details.

In calculating flux we have assigned a weight to the data from each mooring on the assumption that it represents the vertically averaged flow between the mid-points to adjacent moorings or to the adjacent shoreline, as appropriate. Via this approach, we calculate that KS02 represents 16% of the total cross-sectional area (about 11.1 km^2), and KS05, KS07, KS10, KS12 and KS14 represent 20%, 23%, 20%, 12% and 8%, respectively. The resultant weighted sum of flow provides a net southward volume flux of 0.57 ± 0.09 Sv (1 Sv = 10^6 m^3 s^{-1}). This flux number includes values interpolated across the 21-km gap based on measured pull-down response of tall moorings at KS05 and KS07. We detail our quantitative analyses to arrive at these adjustments to the measured flows in Appendix C. We emphasize that the 0.57 ± 0.09 Sv value does not include the unknown current above about 30-m depth nor values extrapolated to 15-m above the seabed. Our volume flux estimate thus represents 79% (8.8 km^2) of the total sectional area only. If we assume that our vertically averaged current represents the depth-average current, then the volume flux through the full cross-section would be 0.72 ± 0.11 Sv. We cannot justify this assumption, however, because vertical shear through the thickness of the oceanic surface layer is likely large and seasonally varying.

Our new lower-bound estimate of volume flux from three years of observations is similar to the value estimated by Sadler (1976) (0.6 ± 0.1 Sv) derived from instruments on three moorings during six weeks in April-May 1972. Sadler's data were acquired in Robeson Channel at 82N, 160 km to the north. Both estimates are also similar in magnitude and direction to values from snapshots derived via surveys using vessel-mounted ADCP in August 2003: 0.8 ± 0.3 Sv (Münchow *et al.*, 2006). Removing the effects of varying wind from the four quasi-synoptic velocity cross-sections collected along Nares Strait, Münchow *et al.* (2007) estimated a net southward volume flux of 1.03 ± 0.10 Sv for the first half of August 2003. The 2003 estimates represent 1–2 day snapshots with excellent spatial resolution during one (perhaps anomalous) summer. The Sadler (1976) data represent a snapshot of monthly variability under fast ice in winter. Our new estimate encompasses temporally well resolved variability up to three years, including both summer and winter conditions.

Table 6. Statistical parameters related to the variability of the vertically averaged currents after record-mean, seasonal, and tidal signals are removed. The bias and trend are from a linear fit of the along-channel velocity $U(t) = bias + trend*t$ where the along-channel direction is defined by the orientation angle where time is in years relative to Jan. 1, 2003. Uncertainties are 95% confidence limits in multiple regression according to Fofonoff and Bryden (1975).

Name	R_{maj} cm s^{-1}	R_{min} cm s^{-1}	Orientation degrees	dof –	T_D hours	Bias cm s^{-1}	Trend cm s^{-1} year^{-1}
KS02	6.1	1.0	56.5	277	95	-6.0 ± 0.45	-0.45 ± 0.15
KS10	7.3	3.1	56.0	259	102	-6.1 ± 0.35	-0.35 ± 0.18
KS12	10.0	3.2	53.0	258	102	-4.3 ± 0.43	-0.28 ± 0.25
KS14	13.6	2.1	60.7	491	54	$+4.0 \pm 0.57$	$+0.24 \pm 0.33$

ii. Interannual trends. By least-squares fits to the time series of along-channel speed at each site (Fig. 9) we have computed statistically significant temporal increases in the southward flow below about 30-m depth. The trend is largest near Canada (0.45 ± 0.15 cm s^{-1} year^{-1}) and diminishes towards Greenland where it is 0.24 ± 0.33 cm s^{-1} year^{-1}, indistinguishable from zero (Table 6). These numbers correspond to a $20 \pm 10\%$ in the sectionally averaged southward velocity between 2003 and 2006.

c. Seasonal time scales: S_{sa} and S_a

The solar annual S_a (365.26 days) and solar semi-annual S_{sa} (182.62 days) astronomical periods describe temporal changes in the gravitational tidal potential due to the sun's declination and distance. However, meteorological effects at these periods also influence large scale forcing via wind, pressure, and sea level. Meteorological factors likely dominate ocean circulation, because the tidal potential at these two periods is small (Neumann and Pierson, 1966).

The periodic motion of S_{sa} and S_a period is strong and co-linear with the shoreline along both coasts, 2.3 cm s^{-1} near Ellesmere Island and 4.3 cm s^{-1} near Greenland. Signals at intermediate locations are smaller, with appreciable variance on their minor axes (not shown). The semi-annual flow is weaker by a factor of 2–4 relative to the annual signal. However, as almost a first harmonic of the annual cycle it contributes to asymmetry of flow as shown in Figure 11. The along-channel, vertically averaged flow near Ellesmere Island has a southward pulse from January through June and a slowly diminishing flow during the remainder of the year. Near Greenland the situation is reversed: a rapidly changing flow occurs from July through December while a more slowly changing flow occurs from January through June. Hence the northward flow near Greenland is most pronounced during summer and the southward flow near Canada is most pronounced during winter. The oscillations are not in phase; the annual signal near Greenland leads that near Canada by about 6 weeks (Fig. 11).
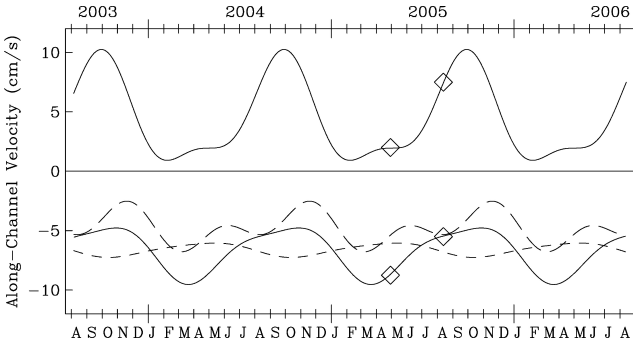
Figure 11. Sum of solar annual, solar semi-annual, and mean along-channel currents for KS02 (solid negative), KS10 (short dash), KS12 (long dash), and KS14 (solid positive). Symbols denote the time of the MODIS images shown in Figures 4 and 3 for April 29 and August 12, 2005, respectively.

d. Daily to monthly time scales

Defining sub-tidal currents as motions with frequencies <0.8 cpd (>1.25 days), we show in Figure 12 the cumulative variance distribution (normalized by the total sub-tidal variance of 26.3 cm^2 s^{-2}) that we derive from the power spectrum shown in Figure 7. It indicates that
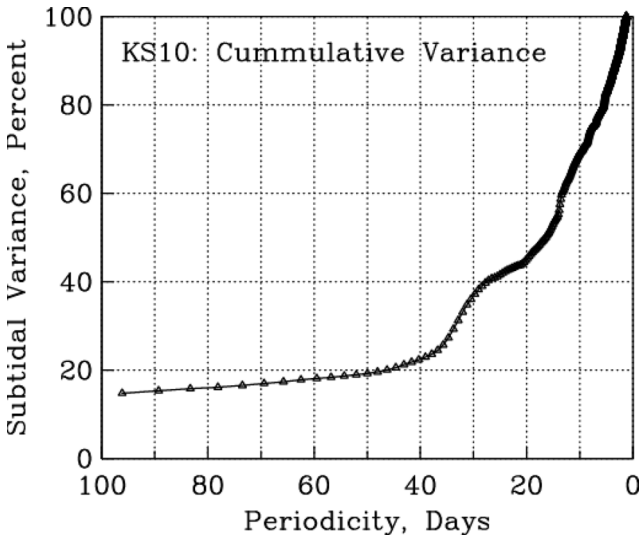
Figure 12. Sub-tidal variance as a function of periodicity. It represents a cumulative integral of the power spectrum of vertically averaged current shown in Figure 7. Note both the slowly increasing variance from periodicities of 100-40 days and the rapid increase for periods between 40 and 30 days. The latter indicates a large amount of kinetic energy near 33 days. The variance is normalized by 26.3 cm^2 s^{-2} which is the variance contained in the spectra for periodicities >1.25 days (frequencies <0.8 cycles per day).
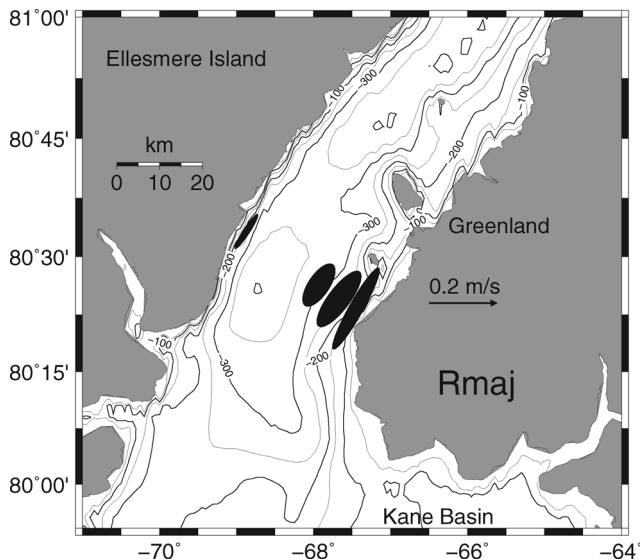
Figure 13. Ellipses of low-frequency variability of vertically averaged current from about 30 m below the surface and 15 m above the seabed. Contours are isobaths in 50-m increments.

more than 80% of the sub-tidal variance is contributed by fluctuations of period less than about 45 days. Furthermore, the kinetic energy density in the band encompassing periods between 1.25 and 45 days is 10.5 cm^2 s^{-2}, equivalent to half of the kinetic energy of the mean flow. This result illustrates that the magnitude of mean flow is larger than the root mean square of the sub-tidal variance. This explains both the small confidence limits for the long-term mean flow (Fig. 10) as well as the rare reversal of sub-tidal currents from their mean direction (Fig. 9).

We can discern spatial patterns in variance within the sub-tidal frequency band via a principal component analysis of the sub-tidal current vectors (Kundu and Allen, 1976). Figure 13 shows that sub-tidal variability increases by almost a factor of two across the channel, from a minimum of 6.1 cm s^{-1} near Ellesmere Island to 13.6 cm s^{-1} near Greenland. The orientations of major axes agree within 4° of 57°. The minor axes are small (about 15% of the major axes) near the coastlines and larger (42% at KS10) near the center of the channel. Enhanced variability at mid channel may be linked to instability of the baroclinic boundary currents described by Münchow *et al.* (2006, 2007).

5. Forcing

In this section we diagnose possible causes of sub-tidal variations in the flow through Nares Strait. All reference to sea level in this section is dynamically in terms of
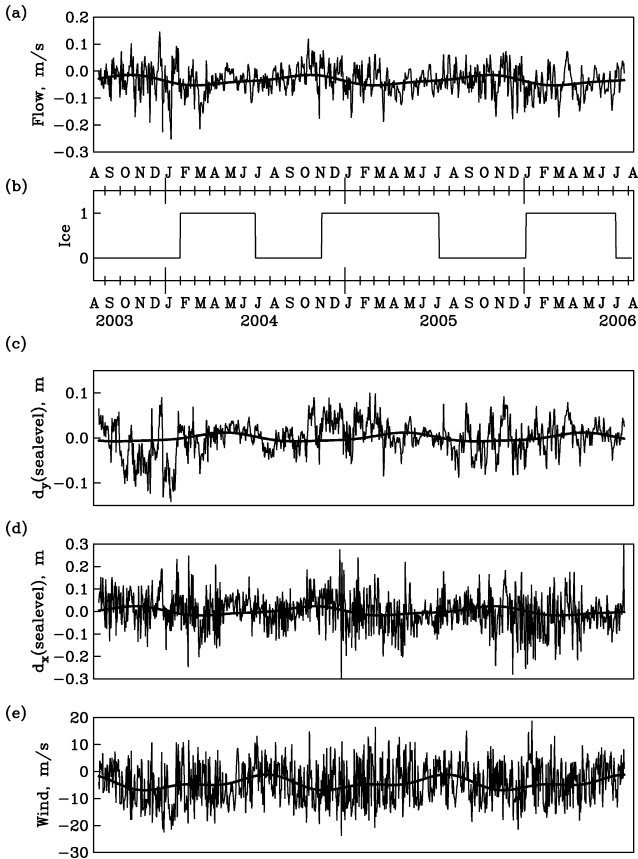
Figure 14. Time series of (a) sectionally averaged along-channel flow (from about 30 m depth to near seabed), (b) ice index, (c) across-channel sea level difference, (d) along-channel sea level difference, and (e) along-channel wind. All properties represent daily averages with the thick solid lines indicating the mean and seasonal signals. The ice index (b) is used to distinguish summer (0) and winter (1) conditions.

hydrostatic pressure anomalies at the bottom. Mean pressures are removed from bottom pressure sensors at Foulke Fjord, Greenland and Alexandra Fjord, Canada while the atmospheric pressure has been added to measurements of sea level at Alert. The analysis below serves as a test on both the quality and adequacy of data needed to estimate dynamical terms. Figure 14 introduces daily averages of the sectionally averaged flow below 30 m along with time series that may relate to the forcing of this flow. An ice index allows us to distinguish between periods of immobile land-fast (winter) and mobile (summer) ice conditions (Fig. 14b) while along- and across-channel sea level difference (Figs. 14c and d) as well as local wind (Fig. 14e) constitute more traditional forcing functions.

a. Across-channel pressure gradients

We expect geostrophy to hold at low frequencies for the across-channel momentum balance that relates along-channel flow U (below 30-m depth of the surface and 15 m above the seabed) to across-channel pressure gradient, e.g.,

$$U = \frac{g}{f}\partial_y\eta \qquad (1)$$

where $U = U(t)$ is the sectionally averaged flow as a function of time t, g is the constant of gravity, f is the Coriolis parameter, and the across-channel sea level gradient (pressure gradient) is $\partial_y\eta \approx \Delta\eta/\Delta y$ where $\Delta\eta = \Delta\eta(t) = (\eta_2 - \eta_1)$ and $\Delta y = (y_2 - y_1)$ estimated from observations $\eta_1(t)$ and $\eta_2(t)$ at two stations a distance $(y_2 - y_1)$ apart.

Figure 14c shows the time series of pressure difference between Foulke Fjord, Greenland (η_2) and Alexandra Fjord, Ellesmere Island (η_1). These two stations are about 200 km to the south of our velocity section. The observations indicate that the sea level difference is always less than 0.1 m except during the 2003/04 winter when southward flow exceeded 20 cm s^{-1} (Fig. 14a). A stronger southward flow corresponds to a decrease in sea level near Greenland relative to Ellesmere Island consistent with geostrophic theory. Using g $=$ 9.81 m s^{-2}, $f = 1.44 \times 10^{-4}$ s^{-1} and $\Delta y = 40$ km, and assuming that the across-channel pressure difference is constant along the channel, we expect a regression line $U = a + b * \Delta\eta$ with $a = 0$ and $b = g/(f\Delta y) = 1.7$ m s^{-1} m^{-1} if U represents the averaged flow in geostrophic balance with the across-channel sea level difference. We conduct a frequency domain correlation analysis by calculating Fourier transforms of $U(t)$ and $\Delta\eta(t)$. We find large variations in correlation with frequency (Fig. 15).

At periods from 3–14 days (0.07–0.25 cpd) the correlated variance is near 70% (Fig. 15a) with a gain close to the expected geostrophic value 1.7 m s^{-1} m^{-1}(Fig. 15c) . At a 30–40 day times scale (0.04 cpd) all locations show significant correlations. At this time scale the gain or transfer coefficient b is about 1 m s^{-1} m^{-1} (Fig. 15c). The phase angle of 30 degrees indicates that the flow leads the sea level gradient by about 3 days and corresponds to a velocity scale of about 0.8 m s^{-1} (200 km over 3 days). We speculate that it is close to a baroclinic pertubation propagating from north to south, e.g., the phase speed of a baroclinic Kelvin wave c $= \sqrt{\Delta\rho g D/\rho_0} \approx 1.4$ m s^{-1} for a density difference $\Delta\rho = 2$ kg m^{-3}, a vertical scale of motion $D = 100$ m, and a mean density $\rho_0 = 1026$ kg m^{-3} (Münchow *et al.*, 2007).

b. Along-channel pressure gradients

A second diagnostic relates to the along-channel momentum balance. Our goal is to determine which physical processes require more focused and dynamically motivated analyses. Possible candidates of a linear, sectionally averaged balance include local acceleration $\partial_t U$, along channel pressure gradient $g\partial_x\eta$, and frictional stresses, e.g.,

$$\frac{\partial U}{\partial t} = -g\frac{\partial\eta}{\partial x} + \frac{\tau^{(x)}}{\rho_0 H} - rU \qquad (2)$$
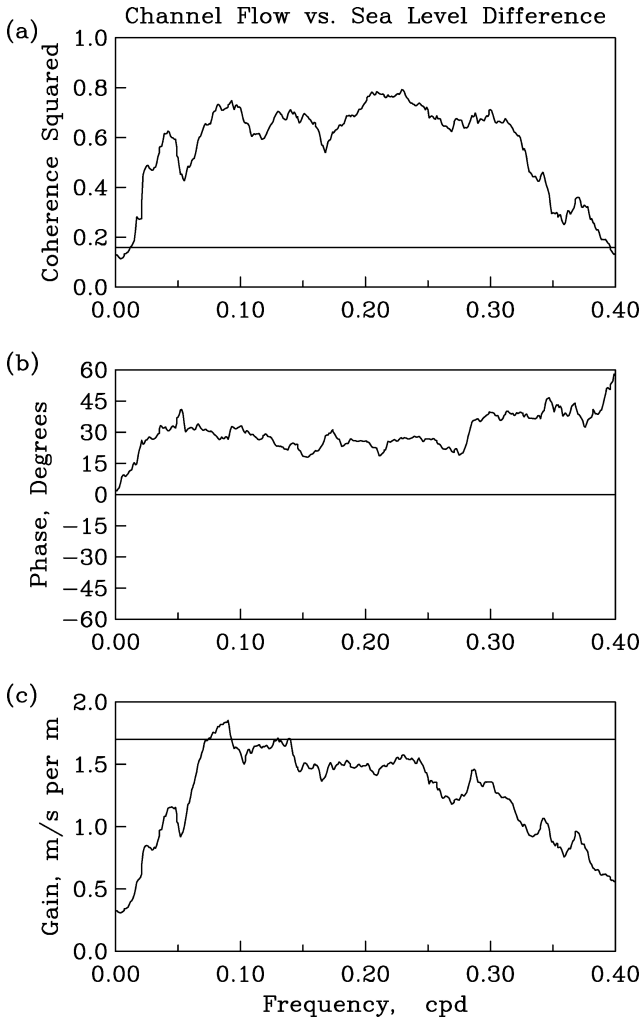
Figure 15. Frequency domain correlation of sectionally averaged along-channel flow (from about 30-m depth to near seabed; Fig. 14a) and across-channel sea level difference between Foulke and Alexandra Fjords: (a) magnitude of the coherence squared (solid line represents 95% confidence limit), (b) phase (flow leads sea level difference), (c) magnitude of the transfer function. The expected value for a geostrophically balanced flow in (c) is 1.7 m s^{-1} per m.

where $\tau^{(x)}$ is the ice-ocean stress in winter and wind-stress in summer, r is a linear friction coefficient, ρ_0 is a reference density, and H the mean water depth. For example, no significant correlation exists between wind stress and flow in both time and frequency domain analyses at any lag or phase (not shown). Hence, from a three-year statistical perspective, the wind

stress has no impact on the section-averaged flows below 30-m depth at sub-tidal time and space scales.

More revealing is a frequency-domain analysis of the flow U with the along-channel pressure difference. We estimate the pressure difference using the total (atmospheric plus ocean) pressure anomaly at Alert in the north and the average of the total pressure anomalies from the bottom pressure records at Foulke and Alexandra Fjords in the south (Fig. 14d). Eq. (2) suggests two possible responses of the flow with regard to pressure difference: the two variables are either in phase (friction) or 90 degrees out of phase (acceleration). Note that both the seabed and the land-fast ice-cover are frictional surfaces. Furthermore, the static ice cover in winter has large roughness elements associated with ice ridges and varying floe thickness.

Figure 16 reveals a dramatic single peak in the coherence near 31-days (0.032 cpd) where 70% of the variance of sea level difference relates to the flow variance at near zero phase. Equally dramatic is the spectral gap between 0.05 and 0.1 cpd (10–20 days). The response at the 30–40 day time scale relates to friction rather than acceleration because of the near zero phase. If we repeat the calculation with a quadratic rather than a linear friction law, the results (not shown) are almost identical with regard to the coherence peak and phase. Over the remainder of frequencies, the interpretation is less clear. While the results are statistically significant in the frequency range from 0.15 cpd (7 days) to 0.3 cpd (3 days), the phase of these correlations varies between 0 and 45 degrees suggesting that both acceleration and friction may contribute to the dynamics.

6. Discussion

We have described almost full-depth observations of currents during a three-year period of continuous observations from 2003–06 in Nares Strait. Challenges included access to this remote location at 80.5N latitude, a harsh climate with intense storms that destroyed our project's camp in the spring of 2005 (Samelson and Babour, 2008), difficult ice conditions in summer navigation by icebreakers, and a weak horizontal geomagnetic field that renders magnetic compass useless. We approached these challenges with (a) a torsionally rigid mooring that held the ADCP on a fixed azimuth during deployment (Fig. 6), (b) a design to provide battery power to all electronic components for 3–4 years, and (c) a selection of a study section wherein deterministic tidal currents could be used to accurately estimate mooring orientation on the sea bed and thus current direction (Appendix A).

Our failure to recover three adjacent ADCP moorings within a 21-km gap posed a challenge that we did not anticipate. Fortunately, four tall moorings within this gap were recovered (see Fig. 5 for locations) and the record of pressure from the instruments at 30-m nominal depth was exploited to derive estimates of current via hydrodynamic analysis of their pull-down response to current (Appendix C).

Our primary goal has been a descriptive regional oceanography in terms of vertically averaged current flowing through the 38-km-wide section. Prior efforts in Nares Strait
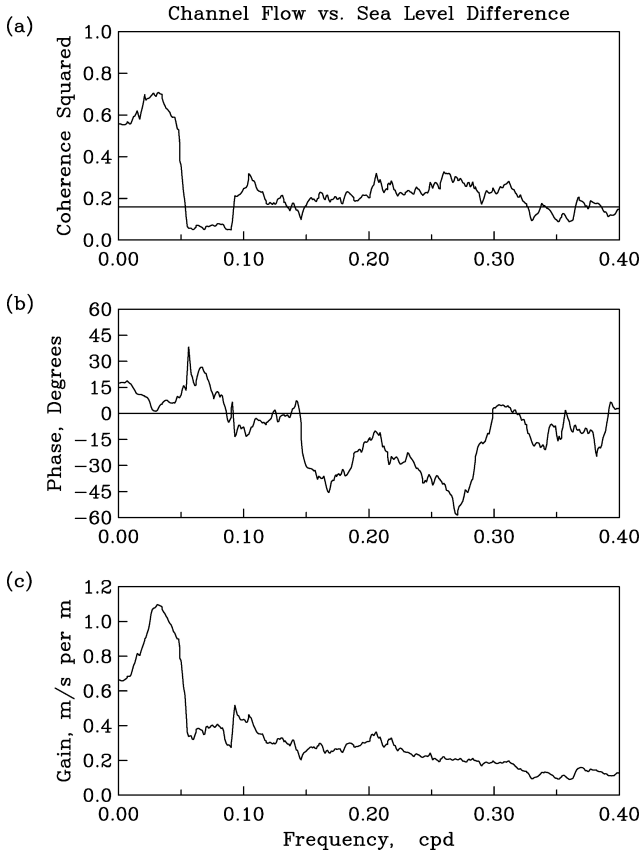
Figure 16. Frequency domain correlation of sectionally averaged along-channel flow (from about 30-m depth to near seabed; Fig. 14a) and along-channel sea level difference between the average of Foulke and Alexandra Fjords in the south and Alert in the north: (a) magnitude of the coherence squared (solid line represents 95% confidence limit), (b) phase (flow leads sea level difference), (c) magnitude of the transfer function.

yielded current records 1.5 months long from three mooring stations in 1972 (Sadler, 1976) and 10 months long from two moorings in 1997-98 (Melling *et al.*, 2001). The monthly snapshot by Sadler (1976) revealed a 0.6 ± 0.1 Sv volume flux while Melling *et al.* (2001) found their data inadequate to form such an estimate.

Our three-year observations at four locations provide an estimated mean volume flux of 0.57 ± 0.09 Sv from the Arctic Ocean into Baffin Bay. This estimate is based on measured currents between about 30 m depth and 15 m above the seabed. This zone represents about 79% of the total sectional area. Our vertical average of flow differs from a full-depth average, because there likely exist strong shear across the fresh-water stabilized oceanic surface layer.

The estimate does include, however, a reasonable estimate of an enhanced flow through the 21 km wide gap in the center of the channel where we derived flow estimates indirectly from measured pull-down of tall moorings (Appendix C). All reported values include both barotropic and baroclinic contributions.

Münchow *et al.* (2006) found that barotropic and baroclinic influences contributed to volume flux in a 1:2 ratio during a two day survey of current and density across our mooring section in August 2003. About two third of the flux was dynamically consistent with geostrophy (thermal wind). In this paper we have tested the geostrophic relation via frequency domain correlation. From the resulting Figure 15 we conclude that a substantial fraction of the sub-tidal along-channel flow is in geostrophic balance and that the along-channel pressure difference is large enough to provide the potential energy for such a geostrophically balanced flow.

Our conclusions implicate the internal Rossby radius of deformation as the dominant dynamical scale of motion

$$L_D = \sqrt{\frac{\Delta \rho g D}{\rho_0}}/f. \tag{3}$$

Here $\Delta \rho$ is a density difference, g is the constant of gravity, D is a vertical scale of motion, ρ_0 is a mean density, and f is the local rate of rotation or Coriolis parameter. The ratio $K = W/L_D$ (W is the channel width) is the non-dimensional Kelvin number that measures the importance of the earth rotation on the dynamics. Garvine (1995) used the Kelvin number to classify freshwater discharges via a careful scaling analysis of momentum and continuity equations.

The Froude number $F = (U/f)/L_D$ emerged as a second parameter that indicates the relative importance of acceleration (Garvine, 1995; Münchow and Garvine, 1993); here U is a sub-tidal along-shore velocity scale. Using published values for Nares Strait (Sadler, 1976; Münchow *et al.*, 2006), Lancaster Sound (Prinsenberg and Hamilton, 2005), and the values for speed reported here, we estimate $K \sim 5$ and $F \sim 0.1$ for the Canadian Arctic through-flow. These dynamical parameters are similar to those of the Norwegian (Mork, 1981) and the Delaware Coastal Currents (Garvine, 1991; Münchow and Garvine, 1993) where density stratification affects much of the water depth, rotational effects are important, and non-linear advection scaled by the Rossby number $R = F/K$ which is small relative to 1. Hence we observe a predominantly linear flow through the Canadian Archipelago that is geostrophically balanced in the cross-channel direction with friction being the dominant control in the along-channel force balance.

In order to be geostrophically balanced, our sectionally averaged flow below 30-m depth requires a 0.02 m difference in sea level across Nares Strait. This value is only about 20% of the observed sea level difference along Nares Strait (Eq. 2, Fig. 15) which is likely the principal driver of the flow. Calculating the coherence between along-channel flow and along-channel difference in pressure, we find a strong peak in correlated variance at

periods longer than 20 days. The near-zero phase at this time scale implicates friction (Fig. 16) because acceleration would generate a 90 degree phase difference. Furthermore, the linear transfer function indicates that a sea level difference of 0.1 m causes a flow of about 0.1 m s^{-1} at monthly period. The situation is less clear at periods shorter than 7 days, because less than 40% of the variance is correlated and the phase at which this correlation occurs indicates a mixed response to friction (zero degree phase) and local acceleration (90 degree phase). We tentatively postulate a primary balance along the channel between pressure gradient and friction at low frequencies (monthly periods) and a balance between pressure gradient, friction, and acceleration at higher sub-tidal frequencies (daily to weekly periods).

Friction influences flow through a seasonally ice-covered channel in several ways. The local wind stress is frictional forcing that is modified by the presence of ice. Using satellite observations of moving ice, Samelson *et al.* (2006) found a strong correlation between predicted wind stress and observed ice movement, which suggests atmospheric control. Münchow *et al.* (2007) found correlation between winds and four snapshots of volume flux during August of 2003. However, our analysis of the three-year long record did not provide statistically significant correlations in either time or frequency domains. Varying ice cover clearly modulates the transfer function for momentum from the atmosphere to the ocean. In the extreme, all ice motion within Nares Strait (and transfer of wind stress to the ocean) ceases when an ice bridge forms between Ellesmere Island and Greenland near Smith Sound (Dunbar, 1973; Kwok, 2005). Figure 4 shows the ice arch on April 29th, 2005. This barrier to all southward ice (but not ocean) flux is established in most years between November and March. Fast ice is a second frictional boundary for oceanic flow until the bridge collapses in late July. Moreover, in the occasional winter when no ice bridge forms, such as 2006–07, there are important implications for the through-flow both of pack ice and seawater. We conclude that future dynamical analyses should be sensitive to the state of motion of ice in Nares Strait. Furthermore, most statistical analyses are based on the presumption that the sampled process is stationary. This is clearly a questionable presumption with the dynamic impact of a non-harmonic seasonally varying presence and state of motion of the ice cover (Figs. 3, 4, 14b).

In summary, friction and its close relation to the ice cover require careful study. Sea ice in Nares Strait alternates between immobility and drift on an quasi-annual cycle. When ice is immobile (fast), the ocean surface velocity is zero by definition, and the ocean is decoupled from the local winds, but not from varying atmospheric pressure. Seasonally variable ice cover introduces variable top-surface friction precisely where buoyant flow is strongest, that is, adjacent to the Ellesmere coast at KS02 where the fastest downstream flow occurs with fast-ice. Under fast-ice the flow near the center of the channel is the slowest (Fig. 11). The situation reverses in summer, with strongest flow near the channel center at KS10. We propose this as evidence for two dynamically different states of the Nares Strait ice-ocean system, one with with buoyant flow hugging Ellesmere Island which may decay into the second through instability introduced by unsteady wind and pressure gradient forcing when

the ice is mobile. Such instability may be less likely when the winter ice-cover provides a steady (frictional) forcing.

Detailed study of frictional effects requires accurate information of current within the frictional boundary layers at the seabed and particularly at the surface. Although an ADCP cannot acquire useful data within the oceanic surface layer where acoustic side-lobe interference from the surface overwhelms the much weaker returns from scatterers in the water, the velocity of the ice (viz. the surface velocity) can be determined via careful processing of the Doppler signals provided that the ice concentration is relatively high. We plan to use Doppler derived surface velocity to estimate current within the surface layer via interpolation between the value at the shallowest depth of measurement and that of the ice itself. This analysis will provide information essential to the calculation of Arctic-to-Atlantic fluxes particularly for freshwater where the contributions of fast-flowing near-surface waters are so strongly weighted by large values of fresh water anomaly in the surface layer.

APPENDIX A

Reference direction

The geomagnetic field in Nares Strait is an unsuitable reference for measuring the direction of current and ice-drift because its horizontal component is weak and variable. We designed a novel torsionally rigid mooring to provide a stable reference direction. The buoyant upper part of the mooring that supported the ADCP was connected to the deadweight anchor via a stiff metal pipe with a universal joint that allowed the instrument to pitch and roll in response to varying current but not to change its heading. The actual heading was arbitrary and unknown, determined by chance when the mooring landed on the seabed. The method of determining the geographic heading of the Doppler sonar is described here.

Tidal current in Kennedy Channel was measured during intervals of several tidal cycles in August 2003 using ADCP mounted on USCGC Healy in conjunction with accurate GPS positioning. Ellipses of measured tidal flow were elongated with cross-channel flows less

than 10% of those along the channel (Münchow *et al.*, 2006). These short-term observations are consistent with simulations using a barotropic tidal model of the marine Arctic at 5-km resolution (Padman and Erofeeva, 2004). Both results justify an assumption that vertically averaged tidal flows measured by the ADCPs on moorings are aligned with their principal axes parallel to that of the channel.

It remains to specify the effective geographic orientation of the channel. We assumed that the predictions of Padman and Erofeeva (2004) provided the dynamically relevant specification. The unknown heading of the Doppler sonar was estimated via vector cross-correlation of simulated and measured tidal flows at the location of each mooring. Observations were prepared for this calculation by filtering to retain diurnal and semi-diurnal variance only. Table 1 provides the correlation coefficients, which exceed 0.94 for all four of the three-year time series. The listed angles are the headings of each Doppler sonar relative to true north.

APPENDIX B

Temporally intermittent observations

Doppler sonar operates via sound backscattered from particles in the water column that are passive to drift with the current. At the 75-kHz operating frequency of the sonar used for this study these particles are large (centimeter sized) zooplankton. Because the abundance of such plankton at given depth varies strongly with vertical diel migration and with seasonal cycles of recruitment and loss, so does the intensity of the echoes received by the sonar. Also, mechanical interactions between ice floes generate noise at 75 kHz that is more intense than the echoes at times of rapid ice movement. By their influence on signal-to-noise ratio, these factors cause intermittency in the time series of valid Doppler derived current. Because such intermittency seriously complicates time-series analysis, we have developed and applied procedures to identify unusable data and to repair resulting gaps in the time series by interpolation.

The procedures involve three successive screens and two techniques for interpolation, applied to the time series from each depth independently. Each value recorded by the instrument was the average of values derived from those pings in the 85-ping ensemble that were judged useful via criteria applied by ADCP firmware.

In the first pass of our post-recovery quality control, data were flagged as reasonable if more than 4 pings contributed to each 30-minute ensemble. Almost all ensembles satisfy this condition at ranges within about 150 m of the ADCP. However, almost a quarter of all ensembles at maximum range are invalid.

In a second step, we used values from those ensembles with more than 64 valid pings to estimate the amplitudes and phases of four semi-diurnal (M_2, S_2, N_2, K_2) and three diurnal (K_1, O_1, P_1) tidal constituents and the mean current via least-squares harmonic analysis. Previously flagged data were then replaced by a value derived from the tidal prediction. Note that this interpolation neglects contributions from non-tidal components of the flow, which are principally at lower frequencies.

The third stage of processing was based on an examination of data within contiguous 24-hour windows of the time series. If there were at least 8 hours of valid data in a window, we used a bi-harmonic spline fit to derive new values for the flagged data. However, if any one spline-interpolated value in the window exceeded 2 m s^{-1} (a very large current) the interpolation was judged unstable and the tidally predicted values in that window were retained.

In summary, there are data of three origins in the final time series: original values judged acceptable, values derived by spline-interpolation to replace invalid data, and values derived via tidal prediction with neglect of non-tidal contributions. The tidal prediction is used least (never more than 10% and generally less than 1%). Spline interpolations approach 15% of all values at maximum range.

APPENDIX C

Spatially deficient observations

No data were acquired by Doppler sonar within a 21-km gap between KS02 and KS10 because the three instruments deployed within this gap (KS04, KS06, KS08, see Table 1) were not recovered. The gap is of great interest because a strong baroclinic jet approximately 10 km wide was observed within it during short-term surveys of ocean current in 2003 (Münchow *et al.*, 2006, 2007). The vertically averaged values of mean current during our three-year observations at KS02 and KS10, which bracket this gap, are almost equal (Fig. 10) and consequently provide no evidence for persistence of this feature, although they do not preclude it. We here present analyses of independent data collected concurrently with our current data to suggest that on average the flow through this mooring gap is at least 15% larger than the flow at KS02 and at least 47% larger than than at KS10.

At deployment in 2003 the KS array incorporated seven short moorings with ADCPs to measure current interleaved with eight tall moorings with sensors to measure temperature, salinity and pressure (Fig. 5). Three ADCPs between KS02 and KS10 were lost, leaving a 21-km gap in the coverage of the section. However, all four tall moorings within this gap were recovered. Information on the current flowing through this gap can be derived via hydrodynamic analysis of the response of these moorings to changing current.

Sea Bird Electronics SBE37 were suspended at nominal depths of 30, 80, 130 and 200 m on each tall mooring. The buoyancy supporting the upper three instruments was deliberately minimal so that the top instrument would be pulled down many tens of metres when current was strong; our motivation was iceberg avoidance. The top instrument measured pressure from which pull-down from resting depth can be determined. The pressure measured by a nearby ADCP at the seabed has been used to correct the SBE37s pressure for changes not related to pull-down, principally tidal and atmospheric variations. Figure 17 presents the cumulative distributions of pull-down distance for adjacent tall moorings at KS07 and KS09. Data during fast and drift-ice periods have been compiled separately and values have been sorted according to the direction of current (80-m depth) measured by the nearest ADCP.
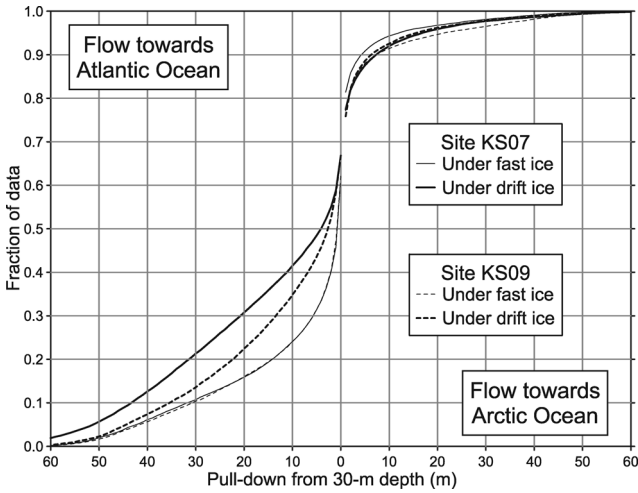
Figure 17. Cumulative distributions of pull-down distance for the top instrument on tall moorings 5 km apart at KS07 and KS09. Values have been sorted and counted progressively from large values accompanying strong south-westward flow, through small values with weak current to large values for north-eastward flow.

Site-to-site differences in pull-down occur primarily with south-westward flow. Comparing KS07 with KS09, difference is negligible with fast ice but appreciable when ice is mobile; pull-down exceeding 20 m is 8% more likely at KS09 than at KS07. Comparing KS05 with KS03, there are differences in both ice states; pull-down exceeding 20 m is 8% less likely at KS05 than at KS03 when ice is immobile but 8% more likely at KS05 than at KS03 when ice is drifting.

Knowledge of the variation of pull-down with current speed is required to link differences in pull-down to differences in current. Pull-down depends upon the distributions of cross-section, buoyancy, drag coefficient and current speed along the full length of a mooring. However because drag (proportional to speed squared) is dominated by high current near the top of the moorings in Nares Strait, we have chosen to explore the relationship between pull-down and current at about 80 m. Figure 18 displays the pull-down of the top instrument of the tall mooring at KS03 relative to the current at KS02, less than 2 km away. Data for south-westward and north-eastward current have been segregated, and, as expected, the curve is symmetric about a pull-down of zero. A very similar result was obtained using the pull-down of the mooring at KS09 in relation to current at KS10, about 3 km distant.

The time-average flows (80-m depth) at KS05 and KS07 have been estimated from pull-down of the tall moorings at these sites via the following procedure. Differences in the occurrence of pull-down exceeding five values spaced between 10 and 35 m were estimated using the curves in Figure 17 for KS05 relative to KS03 and for KS07 relative to KS09; the current associated with each pull-down value was calculated using the fitted
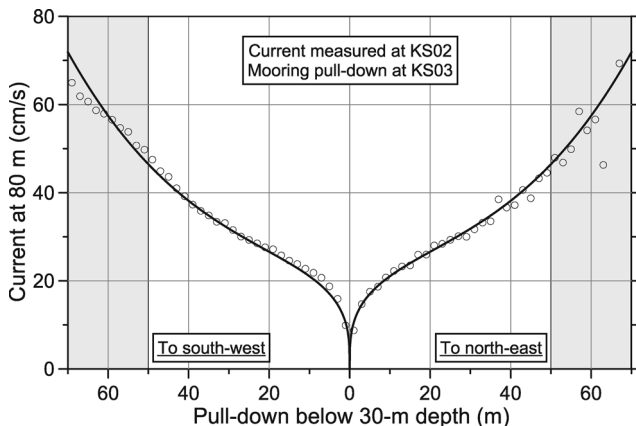
Figure 18. Pull-down of the top instrument of the tall mooring at KS03 relative to the current (80-m depth) measured at KS02, less than 2 km away. Symmetry revealed by separate consideration according to current direction promotes confidence in the derived empirical relationship (thick line).

curve on Figure 18. The cumulative distribution of along-channel current (80-m depth) from the reference station (KS02 for KS05 and KS10 for KS07) was shifted in speed until the difference in cumulative probability between the original and shifted curves matched the difference in pull-down probability for the associated current. The necessary shift is the difference in 80-m depth current between the site in question (KS05 or KS07) and the reference site (KS02/KS03 or KS10/KS09).

Along-channel current at 80-m depth at KS02 averaged -10.1 cm s^{-1}. The pull-down analysis indicates that current at KS05 was -11.6 cm s^{-1}, about 15% stronger than at KS02. Along-channel current at 80-m depth at KS10 averaged -7.5 cm s^{-1}. The pull-down analysis indicates that current at KS07 was -11.0 cm s^{-1}, about 47% stronger than at KS10. It has been necessary to base this analysis on assumptions that current was the same at KS03 where pull-down was measured as at KS02 where current was measured, and similarly in relation to KS09 and KS10. The differences of 1.5 cm s^{-1} in mean current between KS02 and KS05, which bracket KS03, and more substantially of 3.5 cm s^{-1} between KS10 and KS07, which bracket KS09, suggest that these assumptions may not be correct. These estimates from pull-down are likely biased low by these assumptions.

REFERENCES

Battisti, D. S. and A. J. Clarke. 1982. A simple method for estimating barotropic tidal currents on continental margins with specific application to the M_2 tide off the Atlantic and Pacific coasts of the United-States. J. Phys. Oceanogr., *12*, 8–16.

Bendat, J. and A. Piersol. 1986. Random Data: Analysis and Measurement Procedures, 2nd ed., John Wiley & Sons, NY, 566 pp.

Bourke, R. H., V. G. Addison, and R. G. Paquette. 1989. Oceanography of Nares Strait and northern Baffin-Bay in 1986 with emphasis on deep and bottom water formation. J. Geophys. Res., *94*, 8289–8302.

Copland, L., D. R. Mueller, and L. Weir. 2007. Rapid loss of the Ayles ice shelf, Ellesmere Island, Canada. Geophys. Res. Lett., *34*, L21501, doi: 10.1029/2007GL031809.

Curry, R. and C. Mauritzen. 2005. Dilution of the northern North Atlantic Ocean in recent decades. Science, *308*, 1772–1774.

Dickson, R., B. Rudels, S. Dye, M. Karcher, J. Meincke, and I. Yashayaev. 2007. Current estimates of freshwater flux through Arctic and subarctic seas. Progr. Oceanogr., *73*, 210–230.

Dunbar, M. 1973. Ice regime and ice transport in Nares Strait. Arctic, *26*, 282–291.

Dunlap, E. and C. C. L. Tang. 2006. Modelling the mean circulation of Baffin Bay. Atmos.-Oceans, *44*, 99–109.

Emile-Geay, J., M. A. Cane, N. Naik, R. Seager, A. C. Clement, and A. van Geen. 2003. Warren revisited: Atmospheric freshwater fluxes and "why is no deep water formed in the North Pacific." J. Geophys. Res., *108*, 3178, doi: 10.1029/2001JC001058.

Filloux, J. H. and R. L. Snyder. 1979. A study of tides, set-up, and bottom friction in a shallow semi-enclosed basin. Part I: Field experiment and harmonic analysis. J. Phys. Oceanogr., *9*, 158–269.

Fofonoff, N. and H. Bryden. 1975. Density of sea waters. J. Mar. Res., *41*, 69–82.

Garvine, R. W. 1987. Estuary plumes and fronts in shelf waters - a layer model. J. Phys. Oceanogr., *17*, 1877–1896.

—— 1991. Subtidal frequency estuary-shelf interaction – observations near Delaware Bay. J. Geophys. Res., *96*, 7049–7064.

—— 1995. A dynamical system for classifying buoyant coastal discharges. Cont. Shelf Res., *15*, 1585–1596.

Holland, M. M., J. Finnis, A. P. Barrett, and M. C. Serreze. 2007. Projected changes in Arctic Ocean freshwater budgets. J. Geophys. Res., *112*, G04S55, doi: 10.1029/2006JG000354.

Kliem, N. and D. A. Greenberg. 2003. Diagnostic simulations of the summer circulation in the Canadian Arctic Archipelago. Atmos.-Oceans, *41*, 273–289.

Kundu, P. and J. Allen. 1976. Some three-dimensional characteristics of low-frequency current fluctuations near the Oregon coast. J. Phys. Oceanogr., *6*, 181–199.

Kwok, R. 2005. Variability of Nares Strait ice flux. Geophys. Res. Lett., *32*, L24502, doi: 10.1029/2005GL024768.

LeBlond, P. H. 1980. On the surface circulation in some channels of the Canadian Arctic Archipelago. Arctic, *33*, 189–197.

Mardia, K. 1972. Statistics of directional data. Academic Press, New York, NY.

Melling, H., Y. Gratton, and G. Ingram. 2001. Ocean circulation within the North Water polynya of Baffin Bay. Atmos.-Oceans, *39*, 301–325.

Melling, H., T. Agnew, K. Falkner, D. Greenberg, C. Lee, A. Münchow, B. Petri, S. Prinsenberg, R. Samelson, and R. Woodgate. 2008. Fresh-water fluxes via Pacific and Arctic outflows across the Canadian polar shelf, *in* Arctic-Subarctic Ocean Flux, Springer Verlag, Dortrecht, Netherlands, 193–261.

Mork, M. 1981. Circulation phenomena and frontal dynamics of the Norwegian Coastal Current. Phil. T. R. Soc. A, *302*, 635–647.

Münchow, A. and R. W. Garvine. 1993. Dynamical properties of a buoyancy-driven coastal current. J. Geophys. Res., *98*, 20063–20077.

Münchow, A., A. K. Masse, and R. W. Garvine. 1992. Astronomical and nonlinear tidal currents in a coupled estuary shelf system. Cont. Shelf Res., *12*, 471–498.

Münchow, A., H. Melling, and K. K. Falkner. 2006. An observational estimate of volume and fresh-water flux leaving the Arctic Ocean through Nares Strait. J. Phys. Oceanogr., *36*, 2025–2041.

Münchow, A., K. Falkner, and H. Melling. 2007. Spatial continuity of measured seawater and tracer fluxes through Nares Strait, a dynamically wide channel bordering the Canadian Archipelago. J. Mar. Res., *65*, 759–788.

Neumann, G. and W. J. Pierson. 1966. Principles of Physical Oceanography, Prentice-Hall Inc., 545 pp.

Nutt, D. C. 1966. Drift of ice island WH-5. Arctic, *19*, 244–262.

Padman, L. and S. Erofeeva. 2004. A barotropic inverse tidal model for the Arctic Ocean. Geophys. Res. Lett., *31*, L02303, doi: 10.1029/2003GL019003.

Parkinson, C. L. and D. J. Cavalieri. 2008. Arctic sea ice variability and trends, 1979–2006. J. Geophys. Res., *113*, C07003, doi: 10.1029/2007JC004558.

Prinsenberg, S. J. and J. Hamilton. 2005. Monitoring the volume, freshwater and heat fluxes passing through Lancaster Sound in the Canadian Arctic Archipelago. Atmos.-Oceans, *43*, 1–22.

Rignot, E. and K. Steffen. 2008. Channelized bottom melting and stability of floating ice shelves. Geophys. Res. Lett., *35*, L02503, doi: 10.1029/2007GL031765.

Sadler, H. 1976. Water, heat, and salt transport through Nares Strait, Ellesmere Island. J. Fish. Res. Board Can., *33*, 2286–2295.

Samelson, R. M., T. Agnew, H. Melling, and A. Münchow. 2006. Evidence for atmospheric control of sea-ice motion through Nares Strait. Geophys. Res. Lett., *33*, L02506, doi: 10.1029/2005GL025016.

Samelson, R. and P. Babour. 2008. Low-level winds in Nares Strait: a model-based mesoscale clima-tology. Mon. Weather Rev., *136*, 4746–4759.

Serreze, M. C., A. P. Barrett, A. G. Slater, R. A. Woodgate, K. Aagaard, R. B. Lammers, M. Steele, R. Moritz, M. Meredith, and C. M. Lee. 2006. The large-scale freshwater cycle of the Arctic. J. Geophys. Res., *111*, C11010, doi: 10.1029/2005JC003424.

Warren, B. A. 1983. Why is no deep-water formed in the North Pacific. J. Mar. Res., *41*, 327–347.

White, D., L. Hinzman, L. Alessa, J. Cassano, M. Chambers, K. Falkner, J. Francis, W. J. Gutowski, M. Holland, R. M. Holmes, H. Huntington, D. Kane, A. Kliskey, C. Lee, J. McClelland, B. Peterson, T. S. Rupp, F. Straneo, M. Steele, R. Woodgate, D. Yang, K. Yoshikawa, and T. Zhang. 2007. The Arctic freshwater system: Changes and impacts. J. Geophys. Res., *112*, G04S54, doi: 10.1029/2006JG000353.

Yang, J. Y. 2005. The Arctic and subarctic ocean flux of potential vorticity and the Arctic Ocean circulation. J. Phys. Oceanogr., *35*, 2387–2407.